RSC Advances

ROYAL SOCIETY OF CHEMISTRY

PAPER

View Article Online
View Journal | View Issue

Check for updates

Cite this: *RSC Adv.*, 2021, **11**, 22633

Refractive index matched polymeric and preceramic resins for height-scalable two-photon lithography†

Magi Mettry,[a] Matthew A. Worthington,[a] Brian Au,[b] Jean-Baptiste Forien,[a] Swetha Chandrasekaran,[a] Nicholas A. Heth,[c] Johanna J. Schwartz,[a] Siwei Liang,[a] William Smith,[b] Juergen Biener,[a] Sourabh K. Saha[d] and James S. Oakdale*[a]

Received 4th March 2021
Accepted 25th May 2021

DOI: 10.1039/d1ra01733k

rsc.li/rsc-advances

Nanofabrication techniques that can generate large and complex 3D structures with nanoscale features are becoming increasingly important in the fields of biomedicine, micro-optics, and microfluidics. Direct laser writing *via* two-photon polymerization (DLW-TPP) is one such technique that relies on nonlinear absorption of light to form nanoscale 3D features. Although DLW-TPP provides the required nanoscale resolution, its built height is often limited to less than a millimetre. This height limitation is driven by the need to tightly focus the laser beam at arbitrary depths within the photopolymer. This requirement necessitates matching the photopolymer's refractive index to specific values but the required techniques have not been disseminated widely in the open scientific literature. To address this knowledge gap, we test two universal, different approaches to generate refractive index-matched polymeric and preceramic resins and demonstrate their performance by printing of fine submicron features in 3D structures as tall as 2.5 mm. Specifically, we achieve index-matching by mixing commercially-available resins or covalent modification of functional monomers. This work investigates the relationship of voxel shape to RI mismatch, and presents tuning of RI through mixing and covalent modification to a nonconventional material system of preceramic resin which has never been demonstrated before. We demonstrate the material flexibility by generating 3D silicon oxycarbide structures from preceramic resists while simultaneously eliminating the part-height limitation of conventional DLW-TPP.

Introduction

High-resolution nanofabrication has been a driving force for advancements in various fields such as reproductive medicine, micro-optics, and microfluidics.[1–9] There are a wide variety of different lithographic nanofabrication techniques including scanning probe lithography (SPN),[10] directed self-assembly (DSA),[11–17] dot-matrix holography,[17] deep UV (DUV),[18] nanoimprint (NIL),[18] interference,[19] electron beam printing (EBM),[20] and direct laser writing *via* two-photon polymerization (DLW-TPP) techniques. Several reviews have surveyed the field comparing both advantages and disadvantages of each technique.[21,22] Of the many nanofabrication techniques, DLW-TPP has excelled as a method for obtaining three-dimensional (3D) microstructures with defined features well below 1 μm.[23–25] It is important to note that print quality, feature size, resolution (resolvable distance between two features) and ultimately the functionality of the printed part rely not only on the DLW-TPP hardware and laser parameters used for fabrication, but also depend strongly on the photoresist properties.

The finest DLW-TPP features are generally obtained by utilizing high numerical aperture ($NA > 1$) oil immersion objectives. DLW-TPP fabrication can then be performed in a conventional microscopy setup in which the writing laser is focused through an index matched oil and a transparent glass substrate into the photo-responsive resin (Fig. 1a). This method of writing is amenable to a wide variety of materials, including opaque resins, such as those containing carbon fillers.[26] However, in this mode fabrication of taller structures is severely limited by the finite working distance of the objective which sets a hard limit to the sample height. Even before reaching this hard limit, the print resolution deteriorates with increasing print height as the laser beam travels through increasing distances of opaque or refractive index mismatched material.[27–30] These issues have been overcome in part through

---

[a] *Materials Science Division, Lawrence Livermore National Laboratory, 7000 East Ave., Livermore, CA 94550-5507, USA. E-mail: oakdale1@llnl.gov*

[b] *Materials Engineering Division, Lawrence Livermore National Laboratory, 7000 East Ave., Livermore, CA 94550-5507, USA*

[c] *Department of Chemistry, United States Air Force Academy, 2355 Fairchild Drive, Suite 2N-225. USAF Academy, CO 80840, USA*

[d] *George W. Woodruff School of Mechanical Engineering, Georgia Institute of Technology, 801 Ferst Drive, Atlanta, Georgia, 30332, USA. E-mail: ssaha8@gatech.edu*

† Electronic supplementary information (ESI) available. See DOI: 10.1039/d1ra01733k

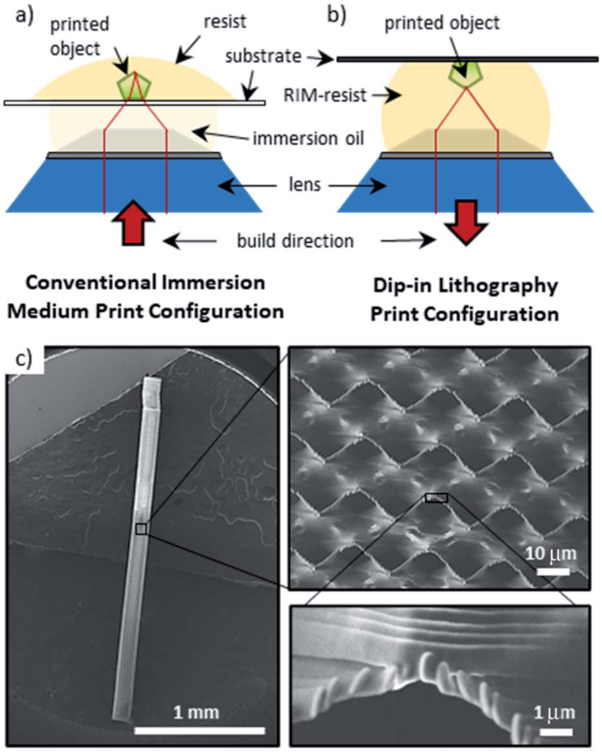

Fig. 1 (a) and (b) Two-photon lithography print configuration modes: traditional immersion medium *vs.* dip-in laser lithography. (c) Scanning electron micrographs of a 2.5 mm tall pillar in the form of a gyroidal lattice printed in dip-in lithography with a photo-resin with a refractive index of 1.52, as described below in Fig. 2.

modified optical setups in which the immersion oil, cover glass and objective move together.[31–34]

The limitations outlined above motivated the development of the so-called dip-in DLW TPP configuration in which the photo-resin is applied directly to the objective (Fig. 1b). Here, the resin has a dual functionality as immersion medium and active resin, thereby ensuring a constant (size and shape) laser beam focal spot throughout the entirety of the built without limitation to the built height, as demonstrated by the 2.5 mm tall gyroidal lattice shown in Fig. 1c. A key requirement for this approach is that the refractive index of the resist must match the refractive index of the immersion medium for which the objective lens was designed.

In this work, we report on two universal approaches to design refractive index matched (RIM) resins for DLW-TPP based on simple mixing of resin components or covalent modification of functional monomers. We have previously implemented similar designs for resins with enhanced radio-opacity[35] and for scalable parallelization of the two-photon fabrication process.[32] Herein, we systematically explore the effects of RI-matching on print quality while qualitatively illustrating the dosage dependence on voxel shape and size. Finally, we show how RI-matching can be utilized to design pre-ceramic resins from thiol–ene modified polyhedral oligomeric silsesquioxane (POSS) monomers to produce ceramic objects with finer features and without height limitations.

Experimental

Materials

All material were used as received. 7-Diethylamino-3-thenoylcoumarin (DETC; Exciton), pentaerythritol triacrylate (PETA; Alfa Aesar, contains 300–400 ppm 4-methoxyphenol (MEHQ) as inhibitor), Bisphenol A ethoxylate diacrylate (BPADA; Aldrich, contains 250 ppm MEHQ as inhibitor), phenylthiol (Aldrich), 1,8-diazabicyclo[5.4.0]undec-7-ene (Aldrich) and acrylo POSS cage mixture (acro-POSS; Hybridplastics). Other solvents (acquired from Aldrich and used as received) utilized for processing and synthesis of the nanofabrication resins described in this work include tetrahydrofuran (THF) dichloromethane (DCM), isopropanol (IPA), triethylamine (TEA), and propylene glycol monomethyl ether acetate (PGMEA).

Formulation of RIM resins: see Table S1†

Polymeric resins were prepared by dissolving 0.1 wt% DETC as the photoinitiator in a mixture of multi-functional acrylate monomers BPADA (RI = 1.545) and PETA (RI = 1.49) of varying ratios. For RI tunability and measurement of each resin see Table S1.†

Formulation of preceramic RIM-resins

Covalent modified RIM-resins. DETC photoinitiator (2 mg, 0.1 wt%) was dissolved in phenolthio-POSS (2 g, RI of 1.52, n = 2.88, where n is the degree of thiol–ene substitution) to yield an optically transparent, viscous photopolymerizable resin.

Mixed RIM-resins. DETC photoinitiator (45 mg, 1.0 wt%) was dissolved in functionalized preceramic phenolthio-POSS (2 g, RI of 1.57, n = 8) and acro-POSS (2.5 g, RI = 1.48, n = 0) yielding optically transparent, viscous photopolymerizable resin with measured RI of 1.52. RI (1.52) was calculated by summing up the RI contributions of each component in proportion to its mass fraction as: (phenolthio POSS wt%) × 1.571 + (acro POSS wt%) × 1.48 = 1.520.

Synthesis of phenolthiol-POSS: see Table S2.†

A 20 mL vial was charged with acro-POSS (2 g, 1.513 mmol), 5 mL of a polar aprotic solvent such as tetrahydrofuran and thiophenol (varied from 2.5 to 8.5 molar equivalents relative to acro-POSS). The reaction mixture was then briefly stirred to achieve a clear homogenous mixture. Then 1,8-diazabicyclo[5.4.0]undec-7-ene (DBU; 20 µL) was added to the reaction mixture resulting in noticeable warming of the reaction vessel – note: the reaction mixture gently boiled for higher equivalents of thiophenol. The reaction was allowed to stir at room temperature for 24 hours before being transferred to a separation funnel. Next, 25 mL water and 40 mL of ethyl acetate were added. The organic layer was collected, washed sequentially with 1 M HCl and saturated brine, and then dried over sodium sulfate. Concentration *via* rotary evaporation, followed by high vacuum yielded an optically clear thiophenol-POSS.

Two-photon lithography setup

Printing was performed on a commercially available Nanoscribe GmbH Photonic Professional GT laser lithography system, powered by a FemtoFiber pro near-infrared laser supplied by TOPTICA and operating with a pulse duration of ~100 fs at a center wavelength of 780 nm and a repetition rate of 80 MHz. Average laser power (mW) was measured before the microscope objective and was varied to control light exposure. Focusing of the laser was accomplished with a Zeiss plan-apochromat 63 × 1.4NA oil DIC M27 objective lens.

General protocol for printing/development

A drop of RIM-resin was applied to the glass substrate ($25 \times 25 \times 0.7$ mm^3) which was first were treated with 3-(trimethoxysilyl) propyl acrylate at 90 °C for 3 min and washed with isopropanol. All structures were printed in the "dip-in" mode. The substrates were then submerged in propylene glycol monoether acetate followed by a bath in isopropanol (IPA) to remove unpolymerized resin after printing. The substrate was then dried either in ambient atmosphere for 24 h or in a Microscopy Sciences 3100 super-critical CO_2 dryer.

General protocol for pyrolysis

The printed green parts were subjected to a heat treatment process where the samples are heated in a tube furnace under nitrogen atmosphere up to 1000 °C at a heating rate of 2°C min^{-1}. Initially samples were heated to 250 °C and maintained at that temperature for 60 min. Subsequently, the samples were heated to 400 °C and maintained at that temperature for 60 min. Then the temperature was increased to 600 °C and held constant at that value for 60 min. From then on to 1000 °C and again held at that temperature for 60 min. Finally, samples were cooled down to room temperature and all the steps were carried out a heating and cooling rate of 2 °C min^{-1}.

General characterization

Nuclear Magnetic Resonance (NMR) spectroscopy was conducted on a 600 MHz Bruker spectrometer in $CDCl_3$. Scanning electron microscopy (SEM) images were obtained on either a JEOL 7401-F scanning electron microscope at 2–3 keV accelerating voltage or a Phenom Pro desktop scanning electron microscope at 5–10 keV. The RI of the uncured photoresist was measured at 20 °C with a Mettler Toledo RE40 refractometer, using the D line of sodium (589.3 nm). For SEM and energy dispersive X-ray spectroscopy (EDS) analysis, samples were coated with ~10 nm of Au–Pd and mounted on an aluminum stub using carbon tape. The estimated probing depth is 10 kV is ~1–1.5 µm.

Point spread function analysis[36]

PSF simulations were preformed using PSF lab software with the following parameters: illumination in the *xz* plane ($y = 0$; units in µm) for a NA = 1.4 oil immersion objective; with a linear polarized light ($\Phi_{\mathrm{BS,ill}} = \pi/4$, $\delta_{\mathrm{ill}} = \pi/2$) of wavelength $\lambda_{\mathrm{ill}} = 780$ nm and with a constant illumination intensity profile $\beta G = 0$ for $a = 0$. Substrate thickness CG = 0.17 mm, working distance $t = t^* = 0.19$ mm.

Results and discussion

Polymer based RIM-resins with a RI of 1.52, designed to match the RI of common immersion oils, were prepared by mixing different acrylic monomers with lower and higher RI values. For example, an approximate 2 : 3 ratio mixture of pentaerythritol triacrylate (PETA, RI = 1.48, see Fig. 2a) and bis-acrylate bisphenol A monomer (BPADA, RI = 1.545) will yield an optically clear viscous fluid with a RI of 1.52. A printable RIM-resin can then be generated through addition of a photoinitiator; DETC photoinitiator is used throughout this work. Fig. 1b illustrates the utility of this particular RIM-resin for generating height-scalable (>1 mm) structures with sub-micron features maintained throughout the built using DLW-TPP dip-in lithography. The relation between the RI of a substance and the polarizability of its molecular components is mathematically described by the Lorentz–Lorenz equation.[37,38] In general, lower indices (RI < 1.4) can be achieved by adding electronegative groups, such as fluorinated moieties,[38] whereas higher indices (RI > 1.7) are obtained by integrating polarizable groups, such as a sulfur and halogens (except fluorine) or by incorporating extended conjugation in the photoresists.[39]

The effect of the photoresist RI value on the print threshold, defined as the minimum laser intensity (I = dosage/laser speed) necessary to generate a freestanding log-pile structure, was studied by systematically changing the PETA/BPADA mixing ratio (Fig. 2b). The initiator concentration (0.1% DETC) was kept constant across the mixing series. Details of the power tests can be found in the ESI (Fig. S2 and S3†). Resins with a RI near 1.52 required substantially lower laser intensities and produced structures with higher quality lattice structures (compare SEM images, Fig. 2b RI 1.495 *vs.* 1.521). The notable asymmetry in print threshold in Fig. 2b is ascribed to different inhibitor concentrations in the individual resin components. Acrylic monomers are stabilized with inhibitors to prevent spontaneous polymerization. Both BPADA and PETA are sold commercially containing 4-methoxyphenol (MEHQ), however in this particular case, PETA contains a 1.4× higher concentration of MEHQ than BPADA therefore the inhibitor concentration decreases with the increase of BPADA wt% relative to PETA thus has a higher print threshold for the same photoinitiator concentration (Fig. 2b).[40,41] Next, point spread functions (PSF) were simulated using PSF Lab software to visual the three-dimensional diffraction pattern of light transmitted through resins with RIs above and below that of immersion oil (*i.e.* 1.518), see Fig. 2c.[36,42] This analysis helps to predict the size and shape of the voxels printed with resins that do not conform with the immersion specifications of the NA 1.4 objective used in this work. We note that this analysis is qualitative in nature due to the non-linearity of two-photon absorption; *i.e.* the size and shape of the voxel would be subject to photoresist-specific thresholds. Furthermore, we measured the RIs of our resins using the D-line of sodium 589.3 nm which are expected to

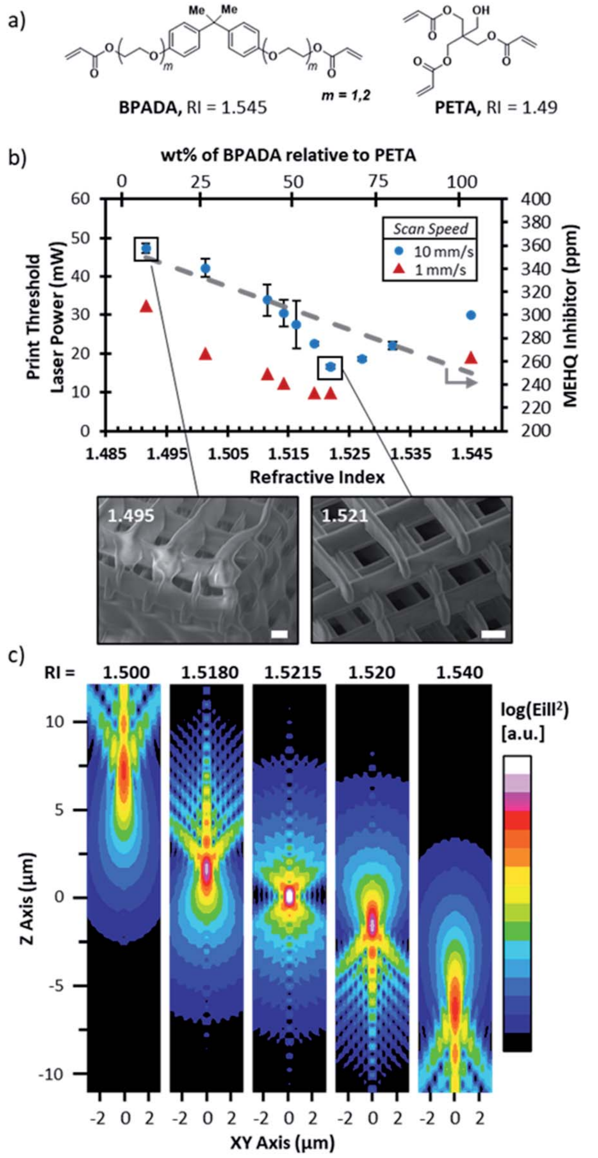

Fig. 2 (a) Pentaerythritol triacrylate (PETA) and bisphenol A ethoxylate diacrylate (BPADA) monomers and their relative RI. (b) Effect of RI on print threshold measured by minimum required laser intensity to arrive at a free-standing part for 10 and 1 mm s^{-1} scan speeds, left axis. Dash line is a linear fit of combination of PETA and BPADA different amounts of methoxy hydroquinone (MEHQ) inhibitor in the used formulation, right axis. The inserts below show scanning electron microscope images (SEM) comparing structures printed with resins with a RI of 1.491 and 1.5215, respectively (scale bars are equal to 1 μm). (c) Illumination intensity profile as function of RI, generated using PSF lab software, where $\log(E_{\mathrm{ill}}^2)$ [a.u.] is the intensity and pattern of light emitted by the two photons source on the resin.[35]

slightly differ from the RIs at the print wavelength of 780 nm. Nonetheless, the PSF results suggest the smallest and most tightly focused illumination will occur with an RI of *ca.* 1.5215 which is the approximate average of the objective design values of the immersion oil and cover slip. The voxel shape predicted at 1.5215 has an aspect ratio of 3 : 1, consistent with experimental results (see SEM images in Fig. 2d and images in Fig. 3). As the RI shifts away from 1.5215, the PSF predicts elongated voxels with aspect ratios of 6 : 1 or greater. At higher illuminations, the PSF further predicts bilobed shaped voxels. Our experimental data are consistent with these predicted trends (Fig. 3 and S3†).

To further evaluate the PSF results as a function of dose ($\text{intensity}^2 \times \text{speed}^{-1}$), we again turned to a series of power tests using the modified log-pile structure shown in Fig. 3a, which was designed to enable head-on imaging of the cross-section of the printed nanowires for the purposes of accurately assessing voxel size and shape. Fig. 3b shows a series of SEM micrographs from a test series printed with a resin with a RI of 1.521 and a constant scan speed of 1 mm s^{-1} as the intensity was systematically increased, from 10 mW to 30 mW. The voxels exhibit a constant 3 : 1 aspect ratio but increased in size with increasing dose; for example, the voxel width grew from 179 ± 19 μm at the print threshold to 552 ± 44 μm at the highest dose (see Fig. S4†). The SEM images also reveal the appearance of wings at higher intensities (dose) resulting in notable height asymmetry (white arrows). These wing-features were apparent in all tested resins, including the RIM resins with a RI of 1.521 at higher energy dosages (Fig. 3c and S3†). Prints using resins with greater mismatches, RI = 1.49 and 1.55, indeed showed the predicted asymmetry with elongated bilobed voxels at higher dosages (Fig. 3c) and wing-features (Fig. 3d). This result implies that the dip-in DLW-TPP can tolerate mis-matched RI-resins if the only goal is to avoid noticeable voxel asymmetries. However, if low aspect ratios are desired, efforts should be made to match the RI of the photoresist to the value for which the objective lens was designed. Finally, if asymmetric voxels are desired, the authors recommend increasing the dosage relative to the print threshold for the index-mismatched resists. One way to achieve this is to decrease the print threshold by increasing the concentration of the photoinitiator.

The simple mixing RIM approach described above requires miscibility between the resin components. However, this is not always easily achievable in practice. Covalent modification of monomers and/or prepolymers with RI-modifying groups serves as an alternative strategy towards RIM-resins. We illustrate this approach using covalently modified polyhedral oligomeric silsequioxane (POSS) to prepare preceramic RIM-resins, see Fig. 4a.

Examples of early preceramic resins for DLW-TPP include work by Pham *et al.*, in which polyvinyl silizane photoresists were printed and pyrolyzed into silicon carbon-nitride (SiCN) microstructures following approximately 41% linear shrinkage.[43] More recent works have explored the formation silicon oxy-carbide (SiOC) from polydimethylsiloxane photoresins.[31,44] Similar pyrolyzable inorganic polymer resins, including POSS, have successfully been utilized in immersion medium print configuration to generate structures mimicing marine diatom coscinodiscus frustules.[45]

However, none of the past studies demonstrated the ability to print in the dip-in mode using index-matched preceramic resins; consequently, the structures were limited to less than half a millimetre in height.

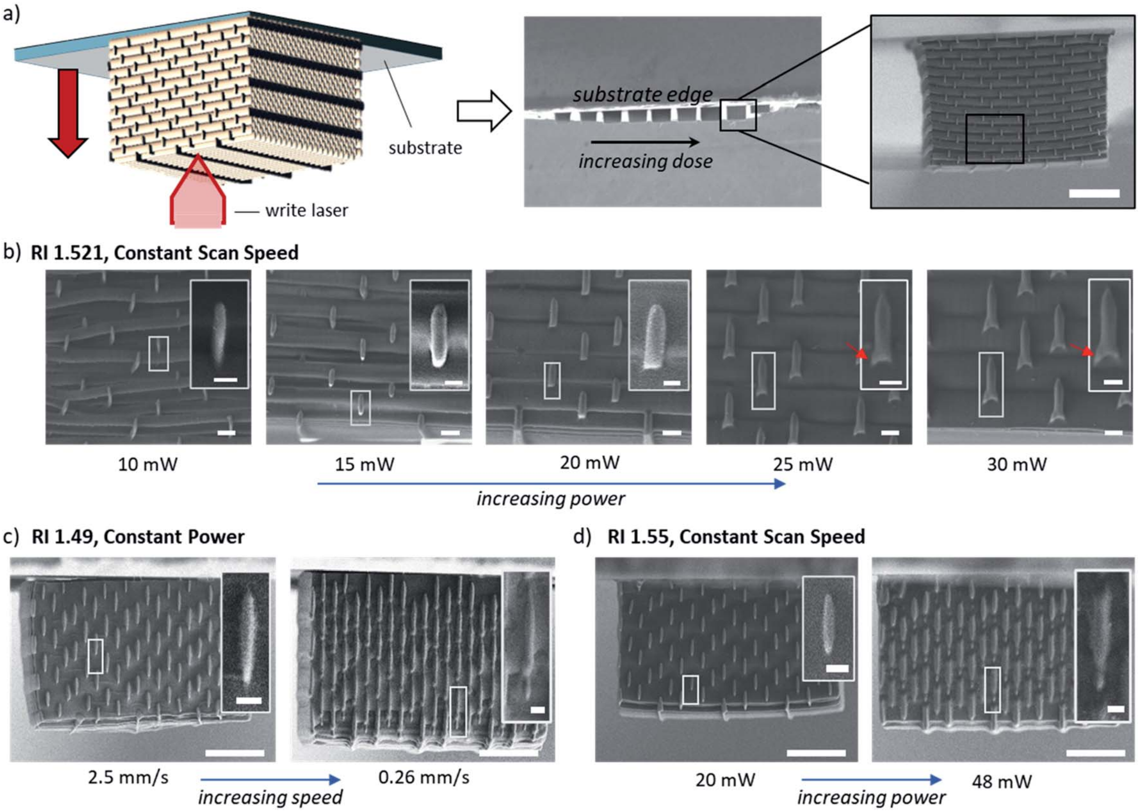

Fig. 3 Comparison of voxel size and shape as a function of dose. (a) Graphical rendering and accompanying scanning electron micrographs of a voxel-imaging test structure, printed on the edge of glass substrate to facility voxel analysis. Red arrow indicates print direction in dip-in lithography mode. Scale bar = 10 μm. (b) SEM images of voxels produced by an RI = 1.521 resin printed at a constant scan speed of 1 mm s^{-1} with increasing peak laser intensity. Scale bar = 1 μm. Inset micrographs highlight the shape of the voxels, scale bar = 0.5 μm. Red arrows indicate 'wing' features. (c) RI = 1.49 resin printed at a constant laser intensity 20 mW with varying scan speed. Scare bar = 10 μm. (d) RI = 1.55 resin printed at a constant scan speed of 1 mm s^{-1} with increasing peak laser intensity. Scale bar = 10 μm. Inset micrographs, scale bar = 1 μm.

Here, using the example of POSS, we present a universal scheme to generate index-matched resists through covalent modification. Preceramic octa-acryl POSS is commercially available and has an RI of 1.48 (Fig. 4a). The pendant acrylate groups in POSS were modified *via* thiol-Michael additions using thiophenol.[46] ^{1}H NMR (Fig. S6†) confirmed that the molar ratio between phenylthiol and the pendant acrylate groups can be tuned ($n = 0$–8, where n is the degree of substitution) to modify the RI between 1.48 and 1.57. RIM preceramic resins with a RI of 1.52 could be formulated *via* precise covalent functionalization, where n is approximately 2.8. Alternatively, the simply mixing strategy could again be employed to arrive at RI = 1.52 using ~1 : 1 ratio of fully functionalized phenolthio-POSS ($n = 8$) combined with unfunctionalized acro-POSS ($n = 0$). Both formulations, each containing 0.1 wt% DETC photoinitiator, performed well in the dip-in lithography configuration, see Fig. 4b for the covalent formulation and Fig. 4c for the physically mixed formulation. Finally, we note that in the physically mixed preceramic formulation, the $n = 8$ phenolthio-POSS derivative no longer contains reactive functional groups and is therefore only physically entrained within the cured material, *i.e.*, $n = 8$ phenolthio-POSS is not covalently attached to the network that results from polymerization of the $n = 0$ acryl-POSS component of the formulation. Non-covalently attached, physically entrained molecules or even particulate fillers are prone to leach from polymeric networks under certain conditions, such as network swelling in the presence of theta solvents. Moreover, non-covalently attached molecules can also act as plasticizers which may unpredictably impact the physical and mechanical properties of the cured material. For these reasons, we generally prefer to avoid the use of modifiers that do not contain reactive functional groups for the purpose of DLW-TPP RIM-resin design. However, in this particular case, the mixture of $n = 0$ and $n = 8$ phenolthiol-POSS RIM-resin performed well under both printing and sintering with no observable indication of $n = 8$ phenolthiol-POSS leaching during printing nor development. We in part attribute the lack of $n = 8$ phenolthiol-POSS leaching to the relatively large size of this molecule (2.2 kDa).

Sintering $n = 0$ and $n = 8$ phenolthiol-POSS RIM-resin at 1000 °C results in formation of a silicon oxycarbide (SiOC) ceramic composite with finer features than their printed counterparts. Pyrolysis results in linear isotropic shrinkage of approximately 35% reducing the feature size from 459 nm to ~240 nm without any indication of cracks. Energy-dispersive X-ray spectroscopy (EDS) data showed a uniformed composition

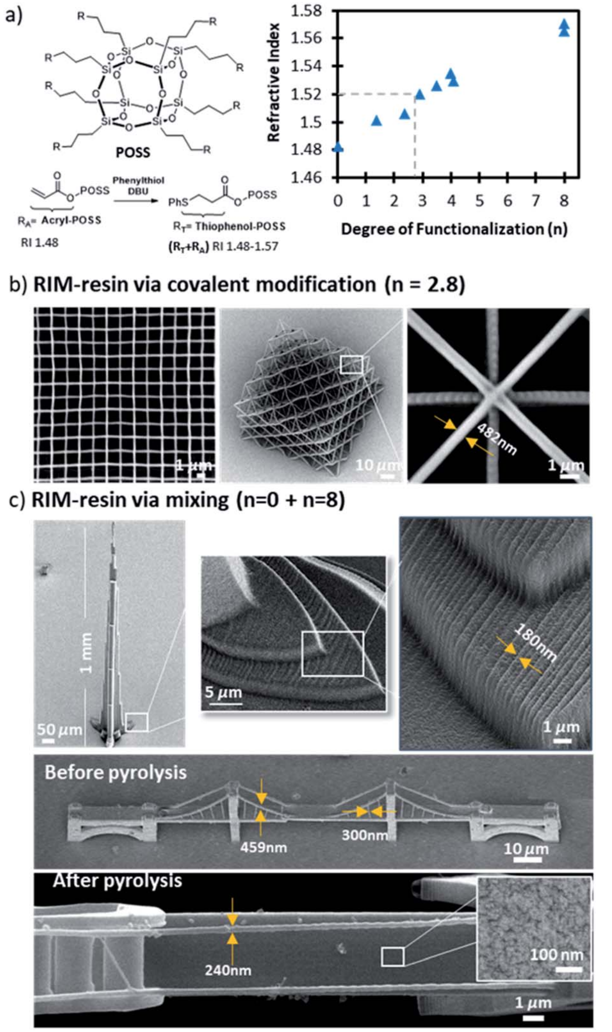

Fig. 4 (a) Polyhedral oligomeric silsesquioxanes (POSS) and functionalization of acryloyl groups *via* thiol-Michael addition with phenolthiol. RI increases linearly with the degree (n) of acryloyl groups functionalization. (b) SEM images of lattice structures from covalent RIM-resin with RI = 1.50 (n = 2.8). (c) SEM images 1 mm tower and a bridge structure with self-supporting cable printed using a RIM-resin prepared from a mixture of n = 0 and n = 8 phenylthiol/acrylo-POSS. Corresponding image of silicon oxycarbide nanobridge following pyrolysis.

of silicon oxy carbide pyrolyzed ceramic nanostructure with 52.54 wt% Si, 14.56 wt% C, and 32.61 wt% O (38.84, 23.6, 37.3 atomic%) which is comparable to the values of other reported SiOC materials values.[47] (see Fig. S5 and Table S3† for full EDS details). While similar SiOC materials have been reported in previous studies, our RIM preceramic resin enables for the first time using the dip-in lithography scheme thereby opening up the route to print mm-tall SiOC structures (Fig. 4c).

Conclusions

In conclusion, we report on two different approaches to generate RIM-resins for fine feature dip-in DLW 2PP structures with no height limitation. We systematically studied the effect of RIM on feature size and voxel aspect ratio. In one appoach, we use a mixture of high RI (BPADA) and low RI (PETA) acrylic monomers to tune the RI and study its effect on the threshold exposure. Supporting PSF simulations were performed to predict the effect of the RI on voxel shape, and generally good agreement was found between experiment and simulation. Both confirm that the smallest and most tightly focused illumination will occur with an RI of proximity 1.5215 resulting in a voxel aspect ratio of 3 : 1. However, even for RIM resins, the voxels adopt a more elongated shape as the laser intensity increases. Using resins with mismatched RI results in both elongated bilobed voxels at higher dosages and the appearance of wing-like features. In the second approach, RIM resins were prepared through covalent modification of RIM monomers. Specifically, we explored the functionalization of acrylo-POSS with thiophenol *via* thiol-Michael addition. The RI is fully tuneable by varying the degree of functionalization of the available acrylic groups of acrylo-POSS (maximum of eight per acrylo-POSS). The resulting preceramic RIM-photoresists enable printing of 3 : 1 aspect ratio voxels and allow print designs with submicron scale features without built-height limitations as seen in Fig. 4c. Post-print pyrolization results in ~35% isotropic shrinkage while transforming the printed green body into a SiOC ceramic. While we have demonstrated RI tuning on two specific resin systems for the dip-in DLW 2PP application, we note that there are other print technologies and applications that are expected to benefit from the resin development described in this work. Especially the covalent functionalization opens the door to functional photoresists for biological and catalysis application while at the same time providing the best possible print performance and longest shelf-life. The covalent functionalization also offers a more stable platform for large-volume fine-feature builts that may take more than a day to print as the covalent functionalization prevents loss of higher vapor pressure functional additives.

Author contributions

Magi Mettry: conceptualization (lead); writing – original draft (lead); ceramic resin formal analysis (lead); writing – review and editing (lead). Matthew A. Worthington: printing formal analysis (supporting); Brian Au: dose measurement formal analysis (supporting); Jean-Baptiste Forien: PSF software (lead); Swetha Chandrasekaran: pyrolysis formal analysis (lead); Nicholas A. Heth: formulation analysis (supporting); Siwei Liang: threshold tests formal analysis (supporting); Johanna J. Schwartz: voxel measurement analysis (supporting); William Smith: CAD software (lead); Juergen Biener: supervision (supporting); writing – original draft (supporting); Sourabh K. Saha: supervision (supporting); James S. Oakdale: conceptualization (supporting); writing – original draft (supporting); writing – review and editing (equal), supervision (lead).

Conflicts of interest

There are no conflicts to declare.

Acknowledgements

The work conducted under the auspices of the U.S. Department of Energy by Lawrence Livermore National Laboratory under contract DE-AC52-07NA27344. Funding was available under LDRD project number 18-ERD-004.

References

1 L. Jiang, W. Xiong, Y. Zhou, Y. Liu, X. Huang, D. Li, T. Baldacchini, L. Jiang and Y. Lu, *Opt. Express*, 2016, **24**, 13687–13701.

2 S. Maruo, O. Nakamura and S. Kawata, *Opt. Lett.*, 1997, **22**, 132–134.

3 T. Ergin, N. Stenger, P. Brenner, J. B. Pendry and M. Wegener, *Science*, 2010, **328**, 337–339.

4 N. Muller, J. Haberko, C. Marichy and F. Scheffold, *Adv. Opt. Mater.*, 2014, **2**, 115–119.

5 D. Jang, L. R. Meza, F. Greer and J. R. Greer, *Nat. Mater.*, 2013, **12**, 893–898.

6 L. R. Meza, S. Das and J. R. Greer, *Science*, 2014, **345**, 1322–1326.

7 T. Buckmann, N. Stenger, M. Kadic, J. Kaschke, A. Frolich, T. Kennerknecht, C. Eberl, M. Thiel and M. Wegener, *Adv. Mater.*, 2012, **24**, 2710–2714.

8 A. Liaskoni, R. D. Wildman and C. J. Roberts, *Int. J. Pharm.*, 2021, **597**, 120330.

9 E. Prina, M. H. Amer, L. Sidney, M. Tromayer, J. Moore, R. Liska, M. Bertolin, S. Ferrari, A. Hopkinson, H. Dua, J. Yang, R. Wildman and F. Rose, *Adv. Biosyst.*, 2020, **4**, e2000016.

10 R. Garcia, A. W. Knoll and E. Riedo, *Nat. Nanotechnol.*, 2014, **9**, 577–587.

11 S. O. Kim, H. H. Solak, M. P. Stoykovich, N. J. Ferrier, J. J. De Pablo and P. F. Nealey, *Nature*, 2003, **424**, 411–414.

12 A. Checco, A. Rahman and C. T. Black, *Adv. Mater.*, 2014, **26**, 886–891.

13 C. M. Bates, M. J. Maher, D. W. Janes, C. J. Ellison and C. G. Willson, *Macromolecules*, 2014, **47**, 2–12.

14 M. Behzadirad, M. Nami, N. Wostbrock, M. R. Zamani Kouhpanji, D. F. Feezell, S. R. J. Brueck and T. Busani, *ACS Nano*, 2018, **12**, 2373–2380.

15 S. Ha, R. Janissen, Y. Y. Ussembayev, M. M. van Oene, B. Solano and N. H. Dekker, *Nanoscale*, 2016, **8**, 10739–10748.

16 H. C. Kim, S. M. Park and W. D. Hinsberg, *Chem. Rev.*, 2010, **110**, 146–177.

17 L. Wan, R. Ruiz, H. Gao, K. C. Patel, T. R. Albrecht, J. Yin, J. Kim, Y. Cao and G. Lin, *ACS Nano*, 2015, **9**, 7506–7514.

18 W. Bogaerts, P. Dumon, J. Van Campenhout, V. Wiaux, J. Wouters, S. Beckx, D. Taillaert, B. Luyssaert, D. Van Thourhout and R. Baets, *IEEE Leos Ann Mtg*, 2003, pp. 754–755.

19 C. Lu and R. H. Lipson, *Laser Photonics Rev.*, 2010, **4**, 568–580.

20 C. Korner, *Int. Mater. Rev.*, 2016, **61**, 361–377.

21 W. B. Huang, X. T. Yu, Y. H. Liu, W. Qiao and L. S. Chen, *Front. Mech. Eng.*, 2017, **12**, 99–109.

22 T. Betancourt and L. Brannon-Peppas, *Int. J. Nanomed.*, 2006, **1**, 483–495.

23 A. Ovsianikov, B. Chichkov, P. Mente, N. A. Monteiro-Riviere, A. Doraiswamy and R. J. Narayan, *Int. J. Appl. Ceram. Technol.*, 2007, **4**, 22–29.

24 V. F. Paz, M. Emons, K. Obata, A. Ovsianikov, S. Peterhansel, K. Frenner, C. Reinhardt, B. Chichkov, U. Morgner and W. Osten, *J. Laser Appl.*, 2012, **24**, 042004–042007.

25 W. Haske, V. W. Chen, J. M. Hales, W. T. Dong, S. Barlow, S. R. Marder and J. W. Perry, *Opt. Express*, 2007, **15**, 3426–3436.

26 W. Xiong, Y. Liu, L. J. Jiang, Y. S. Zhou, D. W. Li, L. Jiang, J. F. Silvain and Y. F. Lu, *Adv. Mater.*, 2016, **28**, 2002–2009.

27 M. J. Booth and T. Wilson, *J. Biomed. Opt.*, 2001, **6**, 266–272.

28 S. Wong, M. Deubel, F. Perez-Willard, S. John, G. A. Ozin, M. Wegener and G. von Freymann, *Adv. Mater.*, 2006, **18**, 265–269.

29 H. E. Williams, Z. Y. Luo and S. M. Kuebler, *Opt. Express*, 2012, **20**, 25030–25040.

30 T. Stichel, B. Hecht, S. Steenhusen, R. Houbertz and G. Sextl, *Opt. Lett.*, 2016, **41**, 4269–4272.

31 L. Brigo, J. E. M. Schmidt, A. Gandin, N. Michieli, P. Colombo and G. Brusatin, *Adv. Sci.*, 2018, **5**, 1800937.

32 S. K. Saha, D. Wang, V. H. Nguyen, Y. N. Chang, J. S. Oakdale and S. C. Chen, *Science*, 2019, **366**, 105–109.

33 K. Obata, A. El-Tamer, L. Koch, U. Hinze and B. N. Chichkov, *Light: Sci. Appl.*, 2013, **2**, e116.

34 W. Chu, Y. X. Tan, P. Wang, J. Xu, W. B. Li, J. Qi and Y. Cheng, *Adv. Mater. Technol.*, 2018, **3**, 1700396.

35 S. K. Saha, J. S. Oakdale, J. A. Cuadra, C. Divin, J. Ye, J. B. Forien, L. B. Bayu Aji, J. Biener and W. L. Smith, *ACS Appl. Mater. Interfaces*, 2018, **10**, 1164–1172.

36 M. J. Nasse and J. C. Woehl, *J. Opt. Soc. Am. A*, 2010, **27**, 295–302.

37 H. A. Lorentz, *Ann. Phys.*, 1880, **245**, 641–665.

38 W. Groh and A. Zimmermann, *Macromolecules*, 1991, **24**, 6660–6663.

39 T. Higashihara and M. Ueda, *Macromolecules*, 2015, **48**, 1915–1929.

40 H. Yang and L. J. Lee, *Polym. Compos.*, 2001, **22**, 668–679.

41 G. L. Batch and C. W. Macosko, *Thermochim. Acta*, 1990, **166**, 185–198.

42 B. Richards and E. Wolf, *Proc. R. Soc. London, Ser. A*, 1959, **253**, 358–379.

43 T. A. Pham, D. P. Kim, T. W. Lim, S. H. Park, D. Y. Yang and K. S. Lee, *Adv. Funct. Mater.*, 2006, **16**, 1235–1241.

44 J. Bauer, C. Crook, A. Guell Izard, Z. C. Eckel, N. Ruvalcaba, T. A. Schaedler and L. Valdevit, *Matter*, 2019, **1**, 1547–1556.

45 S. Luo and J. R. Greer, *Adv. Eng. Mater.*, 2018, **20**, 1800301.

46 D. W. Yee, M. D. Schulz, R. H. Grubbs and J. R. Greer, *Adv. Mater.*, 2017, **29**, 1605293.

47 Z. C. Eckel, C. Zhou, J. H. Martin, A. J. Jacobsen, W. B. Carter and T. A. Schaedler, *Science*, 2016, **351**, 58–62.